PNAS RESEARCH ARTICLE | NEUROSCIENCE

BIFROST: A method for registering diverse imaging datasets of the *Drosophila* brain

Bella E. Brezovec[a,b,1], Andrew B. Berger[a,c,1], Yukun A. Hao[a,d,1], Albert Lin[b,e,1], Osama M. Ahmed[b,f,1], Diego A. Pacheco[b,g], Stephan Y. Thiberge[b], Mala Murthy[b,2], and Thomas R. Clandinin[a,2]

Affiliations are included on p. 10.

Edited by Ilona C. Grunwald Kadow, Rheinische Friedrich-Wilhelms-Universitat Bonn, Bonn, Germany; received January 3, 2024; accepted October 13, 2024 by Editorial Board Member Amita Sehgal

Imaging methods that span both functional measures in living tissue and anatomical measures in fixed tissue have played critical roles in advancing our understanding of the brain. However, making direct comparisons between different imaging modalities, particularly spanning living and fixed tissue, has remained challenging. For example, comparing brain-wide neural dynamics across experiments and aligning such data to anatomical resources, such as gene expression patterns or connectomes, requires precise alignment to a common set of anatomical coordinates. However, reaching this goal is difficult because registering in vivo functional imaging data to ex vivo reference atlases requires accommodating differences in imaging modality, microscope specification, and sample preparation. We overcome these challenges in *Drosophila* by building an in vivo reference atlas from multiphoton-imaged brains, called the Functional *Drosophila* Atlas. We then develop a registration pipeline, BrIdge For Registering Over Statistical Templates (BIFROST), for transforming neural imaging data into this common space and for importing ex vivo resources such as connectomes. Using genetically labeled cell types as ground truth, we demonstrate registration with a precision of less than 10 microns. Overall, BIFROST provides a pipeline for registering functional imaging datasets in the fly, both within and across experiments.

Drosophila | registration | connectome | alignment

Significance

Large-scale functional imaging experiments in *Drosophila* have given us new insights into neural activity in various sensory and behavioral contexts. However, precisely registering volumetric images from different studies has proven challenging, limiting quantitative comparisons of data across experiments. Here, we address this limitation by developing BrIdge For Registering Over Statistical Templates, a registration pipeline robust to differences across experimental setups and datasets. We benchmark this pipeline by genetically labeling cell types in the fly brain and demonstrate sub-10 micron registration precision, both across specimens and across laboratories. We further demonstrate accurate registration between in vivo brain volumes and ultrastructural connectomes, enabling direct structure–function comparisons in future experiments.

Calcium imaging studies of neural activity have provided central insights into brain function in multiple model systems, including the nematode *Caenorhabditis elegans* (1–6), the larval zebrafish (7–11), the fruit fly (12–18), and the mouse (19). In order to compare such volumetric imaging datasets across individual animals, data from individual animals are often aligned within a common set of spatial coordinates defining an atlas, an approach that has been widely used in fish, rodents, and humans (20–23). In this approach, the precision with which data can be registered to such a "local atlas" places limits on the effective spatial resolution of aggregated data, defining the spatial scale of quantitative comparisons. As it has proven challenging to precisely register data from different experiments in the same space, these atlases have generally been restricted to the bounds of a single project, where data were acquired using the same experimental apparatus and protocol (24–26). Moreover, cross-modal registration that bridges ex vivo fixed tissue atlases to in vivo atlases has largely defied current methods, limiting comparisons of functional and anatomical measures.

The adult fruit fly *Drosophila melanogaster* is a well-established platform for circuits neuroscience and recent advances have enabled large-scale functional imaging in this system (12, 15–18, 27). Such studies have revealed widespread sensory responses and movement-related neural activity, probed the relationships between neural activity and metabolism, and have led to the discovery of novel circuits. Each of these studies registered volumetric neural activity data either onto an in vivo local atlas or an extant ex vivo fixed-tissue atlas (28–34). However, different in vivo datasets have not been cross-registered, precluding direct comparisons, as well as a wealth of ex vivo neuroanatomical datasets (29), including gene expression patterns (35–37) and synapse-level wiring diagrams (connectomes) (32, 38–40). Cross-registration of these ex vivo resources has enhanced their utility as, for example, spatial registration has allowed morphologically defined cell types identified in the connectome to be associated with specific genetic driver lines (33, 34, 41, 42). However, it has been difficult to align in vivo functional data to ex vivo atlases with cell-type precision (∼5 µm) (12, 15) due to differences in imaging modality, microscope specification, and sample preparation.

The authors declare no competing interest.

This article is a PNAS Direct Submission. I.C.G.K. is a guest editor invited by the Editorial Board.

[1] B.E.B., A.B.B., Y.A.H., A.L., and O.M.A. contributed equally to this work.

[2] To whom correspondence may be addressed. Email: mmurthy@princeton.edu or trc@stanford.edu.

This article contains supporting information online at https://www.pnas.org/lookup/suppl/doi:10.1073/pnas.2322687121/-/DCSupplemental.

Here, we present a robust and generalizable image registration pipeline, BrIdge For Registering Over Statistical Templates (BIFROST), that enables quantitative comparisons in *Drosophila*, across individuals and experimental setups. We created an in vivo atlas, the Functional *Drosophila* Atlas (FDA), that can accommodate functional datasets from different experiments and labs. An in vivo atlas allows us to represent functional activity in a common space which better reflects the geometry of the brain inside the head. We then aligned the FDA with extant ex vivo templates (28–31, 33, 34), thereby importing atlas labels (30), neuropil annotations (30), information from the connectomes (32, 38–40), and powerful tools for neuron identification (33, 34, 41, 42). Using these atlas labels, we demonstrate that our registration pipeline outperforms existing methods (43, 44). We further validate our method by registering in vivo volumes collected on different microscopes in which the same cell types are fluorescently labeled to the FDA. Comparing these datasets in FDA space, we demonstrate that our cross-lab registration is precise to less than 10 microns. We also demonstrate that BIFROST can be used to align partial subvolumes of the brain into FDA space, allowing users the flexibility to image particular regions of interest while retaining the ability to align to the atlas. Finally, we show that our pipeline can be used to register functional imaging data to connectomes with a precision of less than 10 microns. Thus, BIFROST creates a common space for in vivo neural imaging data, provides easy-to-use tools for accurate registration, and enables direct comparisons of functional data and ex vivo anatomical resources.

Results

Overview. Functional imaging datasets collected using fluorescence microscopy often comprise two separate channels, with one channel recording neuronal activity using one sensor (such as a calcium indicator), and one channel recording signals associated with a structural marker that broadly labels the brain. In our approach, the structural signals from individual brains in a single experiment are first registered together to form a template. The warp parameters derived from this transformation are then applied to the neuronal activity channel from each brain, thereby bringing these signals into the template space. Next, templates derived from each experiment or laboratory are aligned to the Functional Drosophila Atlas (FDA), allowing all datasets to be quantitatively compared to each other, and to other resources that are registered to the FDA (Fig. 1).

Developing the FDA. Our goal was to develop an accurate pipeline for registering brain-wide imaging data to a single atlas. In flies, previous work has described atlases that span the entire brain using ex vivo datasets, and as well as atlases that span the central brain in vivo (12, 15, 29, 34). However, no in vivo atlas spanning the entire brain has been described in either sex. To develop an atlas that best captures the structure of the female fly brain in vivo, a widely used model, we sought to suppress both individual and technical variation. To do this, we first imaged each individual brain, inside the head of the living fly, 100 times at a resolution of 0.6 × 0.6 × 1 μm, capturing expression of a panneuronally expressed cell surface marker (myristylated tdTomato) using two-photon microscopy. These 100 volumes were then aligned using linear (affine) and nonlinear (Symmetric Normalization, SyN) transformations, as implemented in Advanced Normalization Tools (ANTs) (43, 44). These were then averaged to define a single volumetric image of each brain that suppressed technical variation in each collected volume. This process was repeated for 30 individuals, and based on a qualitative assessment, 16 were selected for further image processing. Each of these images were normalized, sharpened, and iteratively aligned using linear and nonlinear transformations to construct the FDA (*SI Appendix*, Figs. S1*A* and S2; see *Materials and Methods*).

Registering Ex Vivo and In Vivo Datasets to the FDA. We next tried to align ex vivo resources, including JRC2018F anatomical labels and genetic tools, the hemibrain connectome and the FlyWire Connectome to the FDA (34, 38, 40). This is a challenging registration problem because the statistics associated with these imaging modalities have substantial differences that reflect 1) changes in brain morphology due to physical constraints of the head, 2) distortion created by fixation, and changes in the angle of the imaging axis 3) differences in the spatial distribution of fluorescence signals due to in vivo labeling of cell membranes versus ex vivo immunohistochemical labeling of synaptic antigens and 4) differences in SNR characteristics associated with single and two-photon microscopy, as well as electron microscopy.

We initially attempted these alignments using the linear and symmetric image normalization (SyN) methods as implemented by ANTs (43, 44). ANTs represents the state-of-the-art implementation of diffeomorphic image registration. We selected this algorithm as a starting point as it does not require laborious and error-prone manual labeling of landmark points, has been shown to outperform other algorithms on a wide variety of image datasets, and displays convenient mathematical properties such as consistency and invertibility (45). However, after applying ANTs to align the FDA and JRC2018F, many regions of the brain aligned poorly (Fig. 2).

ANTs uses a mutual information metric to optimize the transformation between two images, a metric that is somewhat robust to cross-modal variance, but which can nonetheless fail when images are sufficiently different. We formalized the mathematical underpinnings of this problem in *SI Appendix*, *Mathematical Formalism of Image Registration*. We therefore sought an alternative registration method that would directly estimate the diffeomorphism that links two images. The majority of modern solutions to cross-modality registration have employed supervised deep-learning approaches. However, these networks require large amounts of training data and may not generalize to out-of-sample images (46–48). Therefore, we instead adapted SynthMorph, an unsupervised, learned contrast-invariant registration method which had the unusual property of being trained on fully synthetic data, theoretically allowing for unbiased cross-modal registration (*SI Appendix*, *Mathematical Formalism of Image Registration*) (49). As we developed the architecture of the BIFROST pipeline, we ultimately demonstrated that registration accuracy was highest when applying the ANTs linear and nonlinear SyN transformations in sequence, followed by SynthMorph (Figs. 1–5). We conceptualize this procedure as ANTs providing a robust initialization which SynthMorph then refines.

For assessing the alignment of in vivo datasets into the FDA, we collected neural activity (nSyb>GCaMP6s; the dependent channel) and anatomical data (nSyb>myr::tdTomato; the registration channel) at brain wide scale in different labs using different imaging systems (Fig. 1 and *Materials and Methods*). To register these datasets to the FDA, we first generated a dataset template by iteratively aligning the anatomical scan from each animal using linear and nonlinear transformations (*SI Appendix*, Fig. S1*B*, see *Materials and Methods*). We then used the combination of linear, nonlinear SyN, and SynthMorph to register these anatomical scans to the FDA. The transformations that align

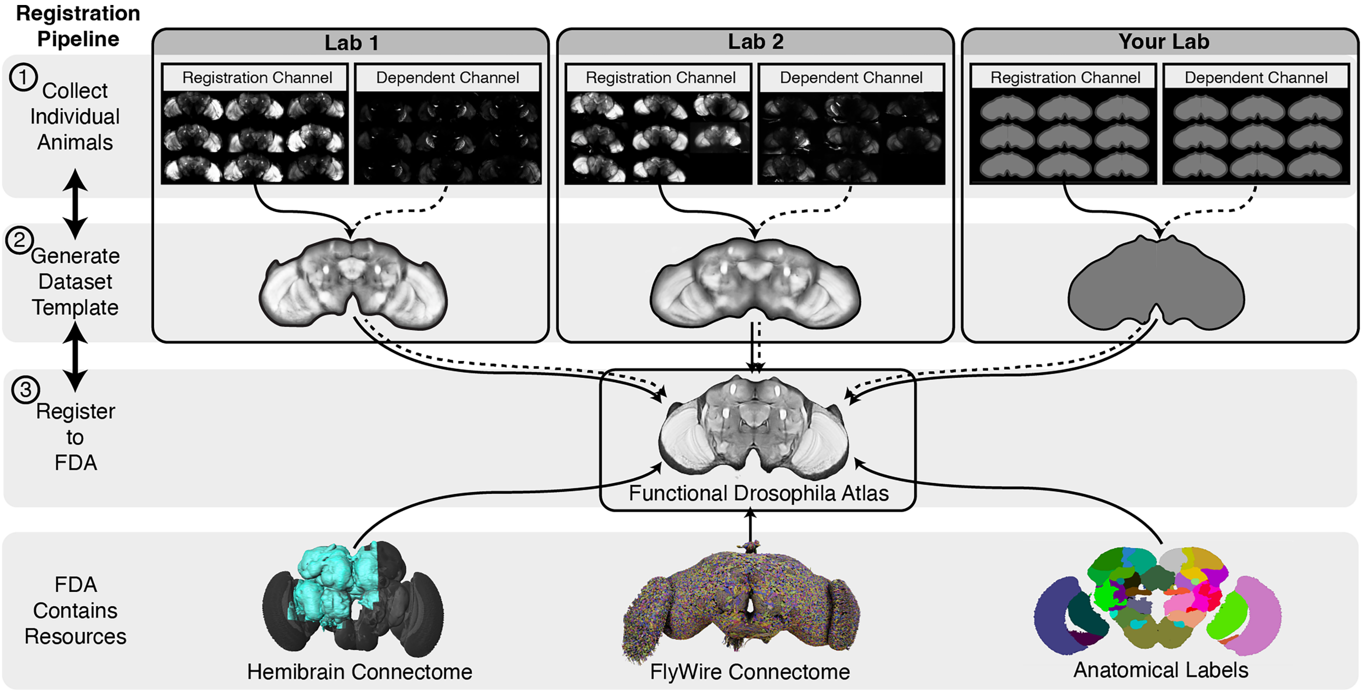

Fig. 1. Overview of the BIFROST pipeline. (Step 1) Collect whole-brain volumetric data from multiple animals, with a panneuronal anatomical label used for registration and an orthogonal-dependent neural activity label. (Step 2) A dataset template is constructed, warping individual brains in the dataset to a common space. The template is constructed from the anatomical channels and the resulting transforms are applied to the neural data to register them into the template space. (Step 3) Dataset templates are registered to the FDA, in which all such datasets can be directly compared. Other resources have been registered to this space, including anatomical labels and connectomes.

each anatomical scan were then applied to the corresponding neural activity data, thereby registering the functional signals to the FDA (*SI Appendix*, Fig. S1*C*; see *Materials and Methods*).

Quantifying Registration Performance. Making quantitative measurements of registration accuracy is challenging (50). To address this challenge, we took two independent approaches. First, we quantified the performance of our method by measuring the overlap of small, well-defined anatomical regions that were manually labeled independently in both the ex vivo and in vivo atlases. Second, we expressed a fluorescent marker in cell-type specific subpopulations of neurons and quantified their alignment within and across labs and to connectomes.

BIFROST Outperforms Existing Methods for Registration Across Modalities. We first quantified registration performance by measuring the alignment of neuropils labeled in the FDA space to the corresponding neuropils labeled in an established ex vivo anatomical atlas, JRC2018F (Fig. 2) (34). Alignment accuracy was quantified for each pair of neuropils using the Sørenson–Dice coefficient, which captures the normalized fraction of voxels that overlap across both neuropil masks (51, 52). For these analyses, we are calculating the transformation using the JRC2018F and FDA templates, and applying the transformations to the neuropil masks. As a control, we first used a linear transform to align the JRC2018F template to the FDA, and achieved an average Sørenson–Dice score of 0.52 (range: 0.13 to 0.75). Next, we added a nonlinear transformation step (SyN), the core nonlinear transformation embedded in the widely used registration pipeline ANTs. However, SyN achieved only a modest increase in performance, with an average Sørenson–Dice score of 0.54 (range: 0.18 to 0.77), emphasizing the challenge of cross-modal registration. However, by adding SynthMorph to complete the BIFROST pipeline and perform the same alignment, we achieved an average Sørenson–Dice score of 0.65 (range: 0.45 to 0.84). We note that precision of registration did not deteriorate with tissue depth (*SI Appendix*, Fig. S3). Thus, BIFROST provides an effective tool for registering signals across the brain.

Quantifying Registration Accuracy Using Sparse Cell Populations. While the Sørenson–Dice coefficient of labeled anatomical anatomical regions of interest (ROIs) is widely used to estimate the precision of registration, this approach also has limitations (50). The stereotyped architecture of the fly brain, combined with cell-type specific genetic labeling, makes possible a quantitative assessment of registration precision, giving access to ground truth measurements that are generally not possible in other experimental systems. We first expressed a fluorescent indicator in a single genetically identifiable cell type, Lobula Columnar 11 neurons (LC11). We chose the LC11 population because LC11 axons converge onto a single glomerulus, facilitating precise estimation of glomerulus position in 3D (Fig. 3 and *SI Appendix*, Fig. S4). This glomerulus lies in the posterior ventral lateral protocerebrum (PVLP) and posterior lateral protocerebrum (PLP), two large neuropils that displayed relatively low contrast in the structural imaging channel. Thus, aligning LC11 within and across laboratories provides a challenging test-case for the BIFROST pipeline. As above, we compared the performance of the BIFROST pipeline to alternative, truncated pipelines that omitted various alignment steps, and included images collected independently in two laboratories (Fig. 3*B*). Each image was from the same strain and expressed the neural activity marker GCaMP6s only in LC11 (as the dependent channel), as well as myristylated-td-Tomato in all neurons (as the structural channel). Qualitatively, individual LC11 glomeruli from both laboratories were similar in appearance after registration (Fig. 3*C*).

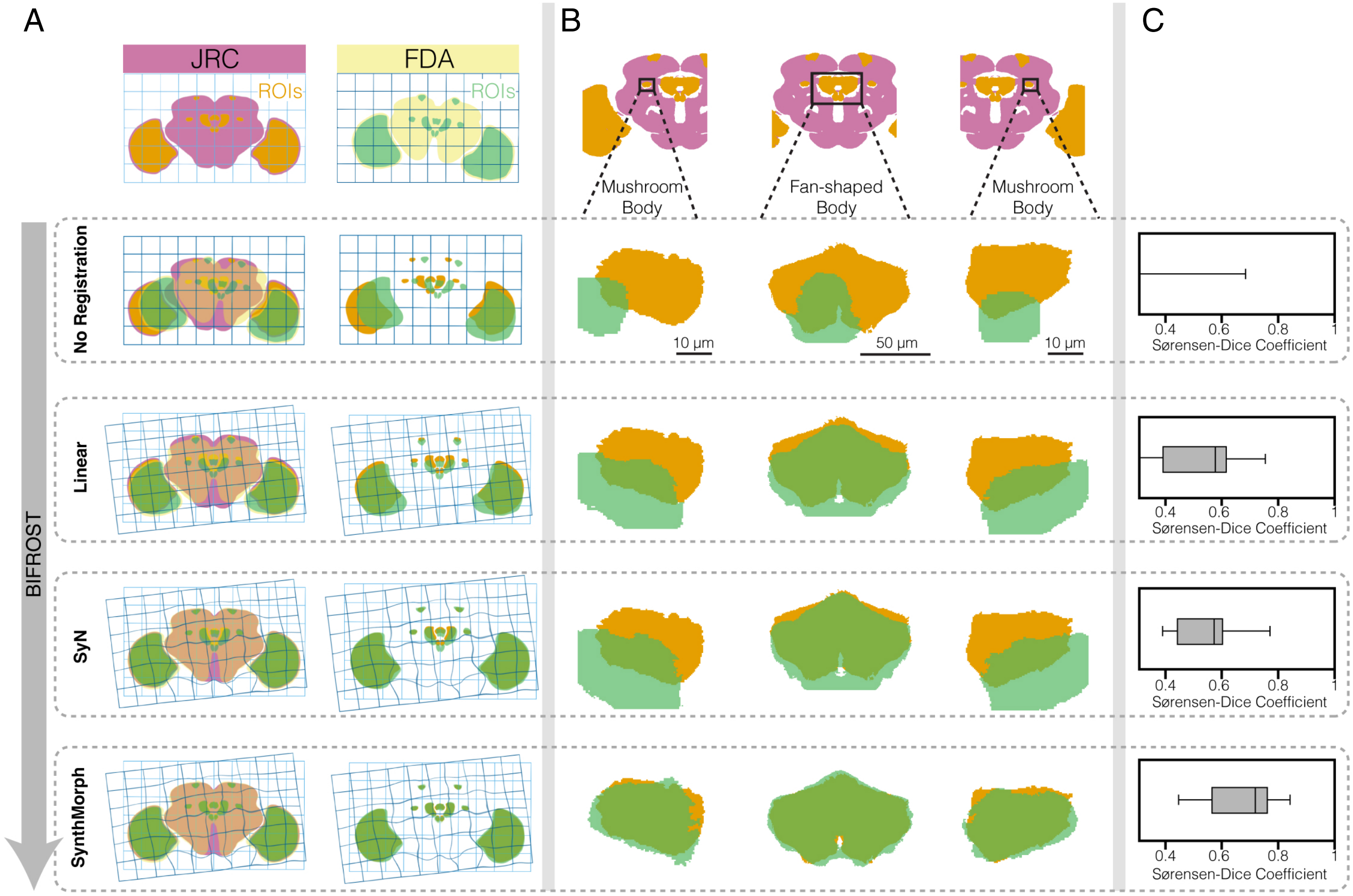

Fig. 2. BIFROST registers neuropils across the brain with high precision. (*A*) Schematization of the registration steps of the BIFROST pipeline. (*Left*) The FDA was transformed into the space of JRC2018F through successive applications of one linear and two nonlinear SyN and SynthMorph steps. (*Right*) The transformations computed at each step were applied to ROI annotations. Only a subset of the 13 labeled ROIs are illustrated. (*B*) Selected neuropil boundaries at successive steps of the pipeline. (*C*) Quantification of neuropil boundary overlap using the Sørenson–Dice coefficient. The box center line indicates median over all neuropils, box limits indicate quartiles, and whiskers indicate minimum and maximum.

We quantified alignment precision by measuring the brain-to-brain variation in the position of the centroid for each glomerulus, independently for both hemispheres, a feature that was robust and not strongly affected by threshold choice (*SI Appendix*, Fig. S4*A*). The average pairwise displacement of any two centroids was 5.2 µm in Laboratory 1, 6.1 µm in Laboratory 2, and 7.3 µm across laboratories (Fig. 3 *D* and *E* and *SI Appendix*, Fig. S4 *B*–*D*). We observed a nearly uniform error distribution, even including along the Z axis (corresponding to the anterior to posterior axis of the brain), the axis that generally suffers most from image distortion (*SI Appendix*, Fig. S4*E*). Notably, the BIFROST pipeline outperformed all truncated variations of the pipeline, particularly for comparisons between labs (Fig. 3*E* and *SI Appendix*, Fig. S4 *D* and *F*). In addition to quantifying LC11 glomerulus registration using measurements of centroids, we manually labeled three additional glomerulus landmarks: the lateral tip, the medial tip, and the stalk. After registration, brain-to-brain variation in the position of the medial tip and the stalk was approximately equivalent to that seen with the centroids (*SI Appendix*, Fig. S4*G*). However, brain-to-brain variation in the position of the lateral tip was increased across all samples, and across labs, all three landmarks were somewhat less precisely aligned than the centroid with an average pairwise displacement of 16.3 µm for the lateral tip, 10.3 µm for the medial tip, and 8.5 µm for the stalk (*SI Appendix*, Fig. S4*G*). Some of this increased variation likely reflects the challenges of manual labeling; however, we also note that the lateral tip of LC11 glomerulus is relatively superficial and might be more affected by variation in the surgical preparation. Nonetheless, as discussed further below, the LC11 datasets derived from both labs aligned well with connectomic resources (Fig. 5).

To test whether this registration precision could be extended to a different brain region, we repeated this experiment using an additional cell population labeled by doublesex (DSX), a neuronal population that extends throughout many neuropils and comprises only fine <10 µm diameter) processes (*SI Appendix*, Fig. S5 *A* and *B*). Again, BIFROST achieved comparable results, displaying 5.5 µm average pairwise displacements between centroids in a readily identifiable structure within the DSX-expressing neuronal population (*SI Appendix*, Fig. S5 *C* and *D*).

Registration of Brain Subvolumes. Many experiments capture neural activity signals from only a subregion of the brain and would benefit from registration across animals. We therefore adapted the BIFROST pipeline to align subvolumes into the FDA (*Materials and Methods*). To test the accuracy of subvolume alignment, we generated a simulated subvolume dataset by selecting a 95 × 95 × 38 µm subregion of one hemisphere from each LC11 brain (Fig. 4). Importantly, this subvolume was not selected from the LC11 template; rather, it was selected independently for each fly, blind to variation in brain orientation and position. We then constructed a subvolume template from

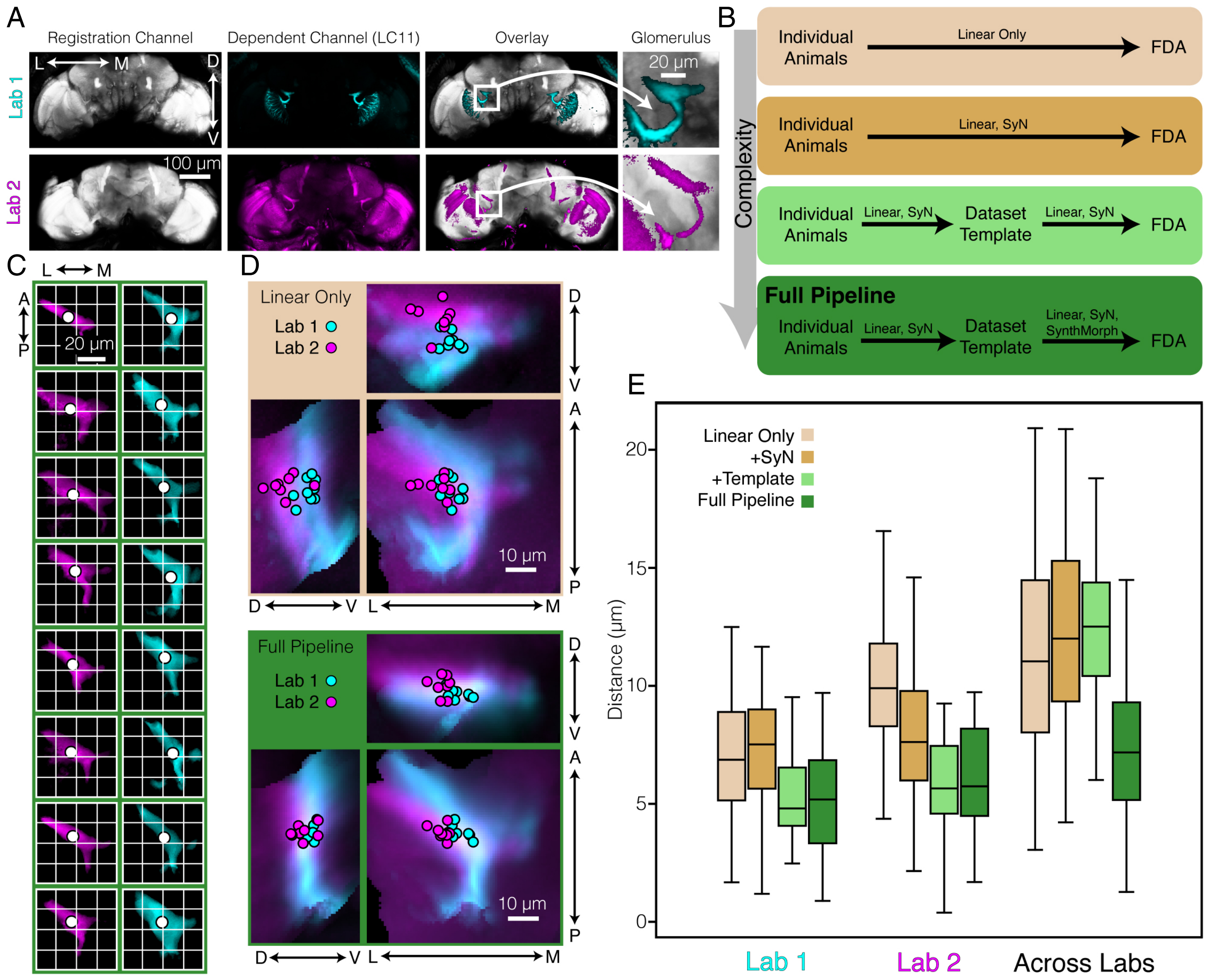

Fig. 3. BIFROST registers brains within and across laboratories. (*A*) A single brain from each laboratory expressing a registration channel (panneuronally expressed myr-tdTomato) and dependent channel (LC11-expressed GCaMP6s). The LC11 glomerulus region is highlighted. (*B*) Schematic flow chart of the BIFROST pipeline, as well as truncated versions that omit individual steps. (*C*) High magnification views of LC11 glomeruli in individual animals from both laboratories after registration into the FDA using BIFROST. The dot denotes centroid of each glomerulus. (*D*), As in (*C*), but individual glomeruli are overlaid and projections along each axis are shown. For comparison, glomeruli transformed by the linear-only pipeline and the full BIFROST pipeline are overlaid(Lab 1 n = 9; Lab 2 n = 8). (*E*) Quantification of the distribution of pairwise centroid distances within and across laboratories, for each pipeline variant. The box center line indicates median, box limits indicate quartiles, whiskers indicate 1.5× the interquartile range.

the individual subvolumes (Fig. 4 *B* and *C*). We aligned this subvolume mean to the FDA using BIFROST (Fig. 4 *D* and *E*) and then assessed the accuracy of alignment as before (Fig. 4 *F*–*H*). We found good agreement between the two sets of aligned data, with an average pairwise displacement between centroids of approximately 6 µm, demonstrating that the BIFROST pipeline can align partial brain volumes to the FDA.

Registration of the FDA with Connectomes. Our goal was to align neuronal morphologies derived from connectomes to the FDA. Prior work has described the coordinate transformations from both the Hemibrain connectome and the FlyWire connectome to JRC2018F (32, 40, 53); therefore, we created a coordinate transformation from JRC2018F to FDA using BIFROST. This allows the coordinates of neuronal skeletons and synapses to be transformed to the FDA space through the path Hemibrain to JRC2018F to FDA, and FlyWire to JRC2018F to FDA. We note that SynthMorph does not provide methods for transforming the coordinates of a point cloud, which is required for a connectome. Therefore, after calculating the SynthMorph transformation, we recalculated it using ANTs (*SI Appendix*, Fig. S1*D* and *Materials and Methods*).

We next examined the accuracy of this coordinate transformation by comparing the positions of the LC11 glomeruli measured in our in vivo datasets to that identified in both the Hemibrain and FlyWire (Fig. 5). Remarkably, this cross-modal alignment was as precise as the alignment across in vivo datasets, with a precision of approximately 5 µm (Fig. 5 *C*–*F*) for LC11, and 7 µm for DSX (*SI Appendix*, Fig. S5*D*). Thus direct comparisons between anatomical wiring diagrams and functional volumetric images are now feasible with high precision.

BIFROST Can Align Diverse Datasets to FDA. To further test the generality of BIFROST, we aligned two additional in vivo datasets to the FDA (*SI Appendix*, Fig. S6). One dataset used two-photon microscopy to image the central brain without

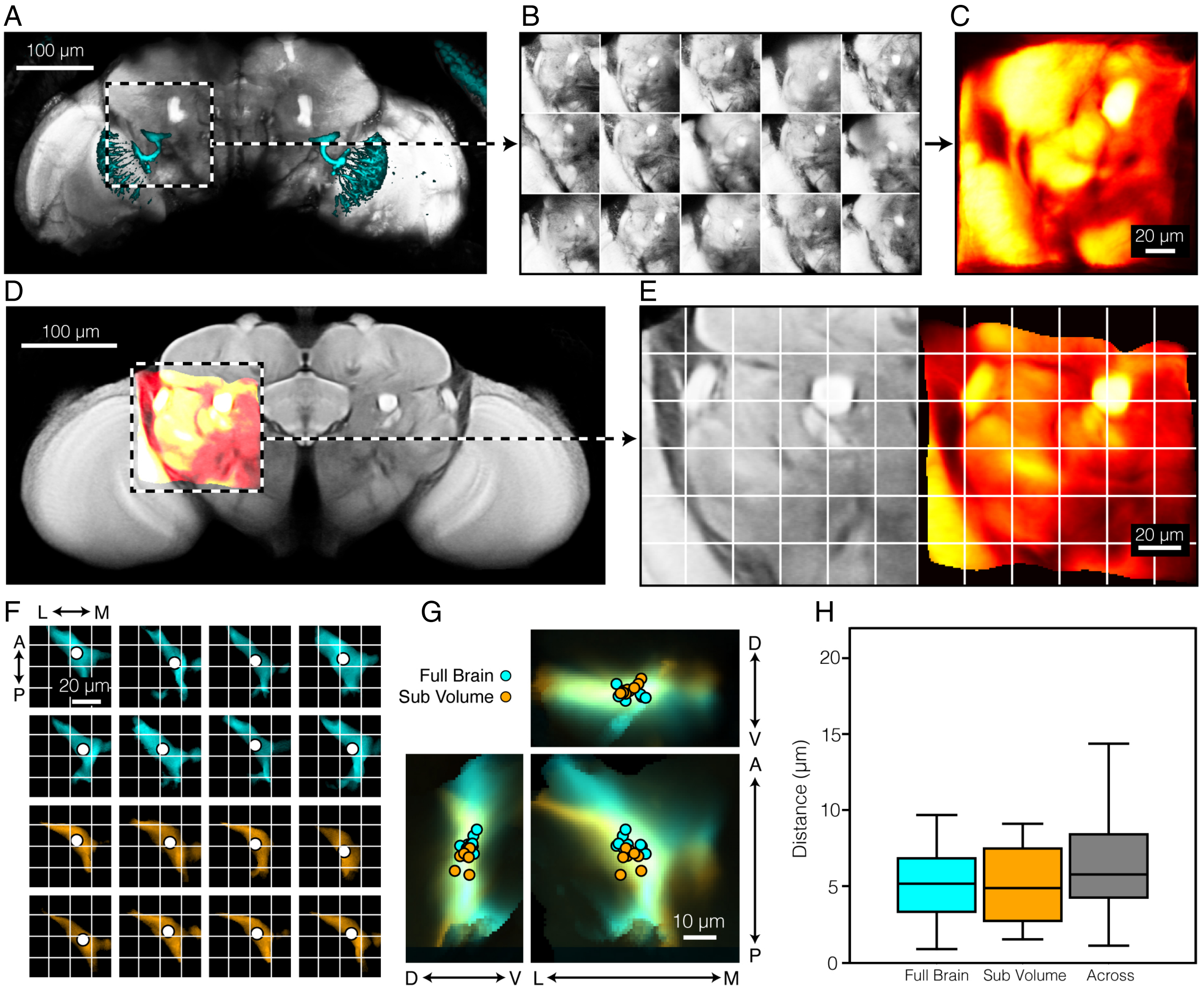

Fig. 4. Subvolumes of the brain can be accurately registered. (*A*) Example fly showing the registration channel (panneuronally expressed myr-tdTomato, gray) and the dependent channel (LC11 expressed GCaMP6s, cyan). The dashed white box indicates LC11 glomerulus region. (*B*) Each brain subvolume from each individual animal. (*C*) The dataset template generated from subvolumes. (*D*) The template subvolume (red) was aligned to the FDA (gray) using BIFROST. (*E*) High magnification view of the aligned mean subvolume. FDA (*Left*, gray) and aligned subvolume (*Right*, red) are shown. (*F*) High magnification view of each LC11 glomerulus after registration to the FDA. Aligned LC11 glomeruli from either the whole brain (cyan) or subvolume imaging (orange). The dot denotes centroid of each glomerulus. (*G*) As in (*F*), but overlaid across animals and projected along each axis. (*H*) Quantification of pair-wise centroid distances after alignment using either the full brain image or the subvolume. The box center line indicates median, box limits indicate quartiles, and whiskers indicate 1.5× the interquartile range.

the optic lobes, along an image axis that was substantially rotated relative to the other datasets we have described (12). The second dataset was collected using light-field microscopy, a fundamentally different imaging modality that combines rapid scanning with relatively low spatial resolution (13, 17). Both datasets displayed qualitatively good alignment to the FDA after processing using BIFROST, demonstrating that BIFROST is robust to both sample orientation and in vivo imaging modality.

Discussion

We developed BIFROST, a pipeline for registering volumetric neural activity data across specimens and in vivo imaging systems. To complement BIFROST, we created the FDA, an in vivo atlas that defines a common space for registering neural datasets. As an additional resource, we also provide the code base needed to generate FDA-like templates. Using genetically labeled neuron populations as ground truth, we show that BIFROST registers neural data across functional datasets at a scale of less than 10 microns, comparable to previous fixed-tissue registrations (54). We further register connectomes, anatomical labels, and genetic resources to the FDA, thereby relating functional neural data to these resources. This toolkit addresses the longstanding challenge of precisely registering brain volumes across experiments and will allow quantitative comparisons of neural activity in *Drosophila* across diverse datasets.

Enabling Comparisons Across Experiments. Comparing signals across experimental conditions and animals is critical for understanding large-scale patterns of neural activity across genetic backgrounds, sensory contexts, and behavioral states. In the fly, large-scale imaging experiments have uncovered brain-wide

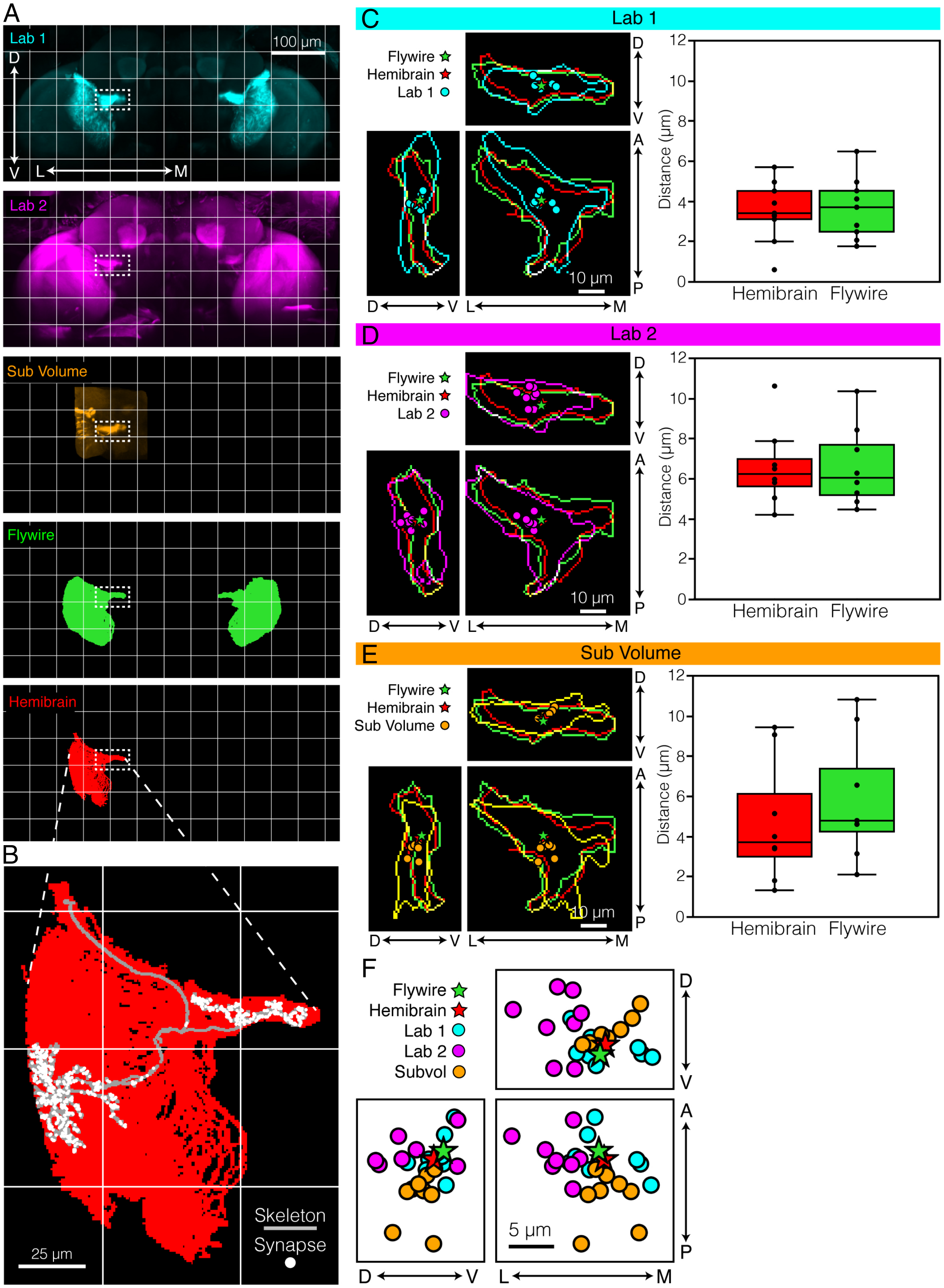

Fig. 5. BIFROST enables registration of connectomes to in vivo imaging data. (*A*) Maximum projections of brains after alignment to the FDA. Template image of the LC11 channel for laboratory 1 (cyan), laboratory 2 (magenta), brain subvolume (orange), LC11 skeletons from the FlyWire connectome (green), and LC11 skeletons from the Hemibrain connectome (red), are shown. (*B*) Example of a single LC11 skeleton and synapses after being aligned to the FDA. (*C*) Comparing alignment accuracy of Laboratory 1 with the Hemibrain and FlyWire connectomes. *Left*: high magnification view of the LC11 glomerulus; projections along each axis are shown. Cyan contour demarks the edges of the template image of LC11 from laboratory 1, while red and green denote the edge of LC11 skeletons from the Hemibrain and FlyWire connectomes registered into the FDA. *Right*: quantification of the distribution of pair-wise centroid distances between each individual LC11 glomerulus and the Hemibrain and FlyWire connectomes. The box center line indicates median, box limits indicate quartiles, and whiskers indicate 1.5× the interquartile range. (*D*) As in (*C*), but for Laboratory 2. (*E*) As in (*C*), but using the subvolume. (*F*) Overlay of LC11 centroids from all brains.

activity patterns correlated with metabolic processes, sensory processing, locomotion, and feeding (12, 14–17, 27, 55). By facilitating statistical comparisons through precise cross-registration of these data types, BIFROST enhances quantitative comparisons of neural activity across conditions, an essential step toward building more comprehensive representations of brain-wide dynamics.

Enabling Function–Structure Comparisons. By achieving precise registration between functional volumes and connectomes, BIFROST allows population-level activity signals to be associated with particular candidate cell types. While previous work in the fly has compared function to structure at the level of brain regions (neuropils) (15, 56), the sub-10 micron alignment demonstrated here will enable function–structure comparisons at an unprecedented spatial scale. For example, this precision will enhance the interpretation of functional data by using the connectome to constrain local and mesoscale cell connectivity, putative neurotransmitters, and labeled cell types (57, 58). Additionally, registering such data at brain scale will enable users to move between testing both small and large-scale circuit and computational models, including those that link neural activity to sensory input, internal states, and behavior.

Improvements Over Existing Methods. The BIFROST pipeline offers several practical and theoretical improvements over existing methods. The most significant theoretical improvement is the pipeline's architecture of initializing the alignment with affine and SyN, followed by fine-tuning with SynthMorph. This is particularly important when aligning datasets across different imaging systems and modalities. BIFROST also incorporates the creation of a Dataset Template, which further increases registration accuracy. Finally, BIFROST has been engineered to seamlessly scale with compute resources, capable of running on a laptop or utilizing the resources of a compute cluster, enabling rapid analysis of large imaging datasets.

Limitations. Although the BIFROST pipeline is flexible with regard to the particular structural marker used, some method to record the anatomical structure of the brain is required. This will mostly likely mean that an imaging channel is reserved for structural measurements of the in vivo brain using panneuronal expression of a fluorescent label, precluding the use of this channel for recording a functional signal.

BIFROST achieves a registration accuracy of less than 10 μm, which surpasses existing methods, but is still nonzero, constraining interpretation of registered data. For example, if in vivo data are collected at single micron resolution, registration will reduce its spatial precision to the 7 μm accuracy of BIFROST. Therefore, any spatial structure that existed in the neural data at a spatial resolution of less than the precision of BIFROST will be blurred. This is particularly important when attempting to assign neural identities based on connectome alignment, where it will typically be impossible to assign a single functional voxel signal to a particular neuron. However, at the same time, if functional signals span multiple imaging voxels, these correlated voxels can be assigned to small populations of candidate neurons that can be functionally validated using other approaches (16). Finally, additional strategies to limit or sparsen expression of the functional effector can likely be implemented in parallel with large-scale imaging to facilitate single-neuron identification (59).

Another class of considerations is biological limitations of alignment precision. Although the fly brain is highly stereotyped, individual brains are not identical. If this individual variation is captured in the structural data, it can be corrected by BIFROST, as long as the differences maintain the same relative positions between structures. However, biological variation cannot be corrected if it exists at a spatial resolution less than the effective imaging resolution defined by the point spread function, if the variation does not affect the labeling method being used to capture brain structure, or if the variation impacts relative spatial positioning of distinct structures. For example, if two structures swapped locations between two individuals, BIFROST would fail to correctly align them.

We further note that the flies used to create the FDA were collected from a particular imaging axis that falls between the anterior–posterior and dorsal–ventral axes. Given the point spread function of the excitation beam inherent in two-photon-microscopy, this results in a slight reduction in imaging resolution along this axis, which is visible from the medial–lateral axis (*SI Appendix*, Fig. S2). Despite this imaging artifact, registration accuracy does not deteriorate along this axis (*SI Appendix*, Fig. S4*E*). Additionally, we note that this imaging axis allows optical access to the entire brain excluding the subesophageal zone which is occluded by the esophagus and is thus not present in the FDA.

Finally, we would like to emphasize a few practical considerations when using BIFROST. First, the accuracy of BIFROST is dependent on the quality of the data being registered. Users should make efforts to achieve optimal and consistent image quality across animals, and avoid, for example, heterogeneous occlusions from tissue or debris, excessive brain motion, excessive bleaching or signal attenuation with tissue depth, brain tearing or mutilation from dissection, or inconsistent structural labeling across animals. Second, we also emphasize the importance of including the correct metadata in your NIfTI image files, in particular voxel resolution and direction. Finally, we also recommend visually inspecting the output of BIFROST, including the dataset template and its alignment to the FDA.

Conclusions

BIFROST, together with the code base for constructing functional atlases, can be adapted for future use in other model organisms. Large-scale functional imaging experiments, as well as whole-brain anatomical studies, are increasingly feasible in many systems, including worms, flies, fish, mice, and primates. Direct comparisons between such functional data and anatomical wiring diagrams have advanced our understanding of computation (3, 60). Moreover, there is broad interest in using connectomic constraints to inform computational models of neural activity (56, 57, 61–63). Tools capable of bridging functional and anatomical imaging modalities via precise volumetric registration will enable finer structure–function comparisons.

Materials and Methods

Genotypes. Flies were grown at 25 °C on molasses (Clandinin Lab) or cornmeal (Murthy Lab) media, and imaged 3 to 5 d post eclosion. The flies used to generate the FDA were *w+/w+;UAS-myr::tdTomato/UAS-GCaMP6f; nSyb-Gal4/+*. The flies used to label LC11 neurons were *w+/w-;nSyb-LexA,LexAop-myr::tdTomato/R22H02-p65ADZp;UAS-GCaMP6s/R20G06-ZpGAL4DBD*. The flies used to label DSX neurons were *w+/w+;brp>STOP>v5-LexA,LexAop-myr::tdTomato/UAS-myr::tdTomato;DSX-FLP,LexAop-GCaMP6s/nSyb-Gal4*.

Mounting and Dissection—Clandinin Lab. Flies were immobilized using a chilled Peltier plate, then fitted into a mount comprising a 3D-printed plastic dish holding a steel shim to secure the head and thorax. To reveal the posterior surface of the head, the head was pitched forward around the medial–lateral axis by approximately 70° relative to the thorax. UV curable glue was applied to the dorsal part of the head, and on the dorsal thorax. A saline solution was added to the dish for dissection (103 mM NaCl, 3 mM KCl, 5 mMTES, 1 mM NaH2PO4, 4 mM MgCl2, 1.5 mM CaCl2, 10 mM trehalose, 10 mM glucose, 7 mM sucrose, and 26 mM NaHCO3). The posterior head cuticle was cut using a tungsten needle and removed to expose the whole brain. Dissection forceps were used to remove fat and trachea.

Mounting and Dissection—Murthy Lab. Flies were chilled on ice and placed in a Peltier-cooled "sarcophagus" held at 4 °C, with the head of the animal restrained in a 3D printed holder. We positioned the head at a 90° angle relative to the thorax and restrained it via UV-cured glue and wax. The holder was then filled with saline (103 mM NaCl, 3 mM KCl, 5 mMTES, 1 mM NaH2PO4, 4 mM MgCl2, 1.5 mM CaCl2, 10 mM trehalose, 10 mM glucose, 9 mM sucrose, and 26 mM NaHCO3), and the cuticle on the posterior side of the head was removed using fine forceps (Dumont 5SF) and a sharp needle. Fat and trachea were removed before imaging.

Two-Photon Imaging—Clandinin Lab. Imaging data were collected using a resonant scanning Bruker Ultima IV system with a piezo drive and a Leica 20× HCX APO 1.0 NA water immersion objective. Either a Chameleon Vision II femtosecond laser (Coherent), or a MaiTai BB (SpectraPhysics) was used to excite GCaMP and tdTomato at 920 nm. A 525/50 nm filter and a 595/50 nm filter were applied to the GCaMP and tdTomato emission photons, respectively. Photons in both channels were collected simultaneously using two GaAsP photomultiplier tubes (Hamamatsu). 100 imaging volumes were collected at $0.6 \times 0.6 \times 1$ μm ($1{,}024 \times 512 \times 241$ XYZ voxels).

Two-Photon Imaging—Murthy Lab. Imaging data were collected on a custom-built 2-photon resonant scanning microscope equipped with a Chameleon Ultra II Ti:sapphire laser (Coherent) and a 25× water immersion objective (Olympus XLPLN25XWMP2). Dissected flies were placed below the objective and perfused with saline. The laser was used to excite GCaMP and tdTomato at 920 nm, with a 520/70 nm filter (Semrock) applied to the green channel and a 617/73 nm filter (Semrock) applied to the red channel. Note, the slightly wider band-pass of this green filter (compared to Clandinin Lab) likely contributed to additional bleed-through of photons from tdTomato, as can be seen in Fig. 3. Photons in both channels were simultaneously collected using GASP photomultiplier tubes (Hamamatsu). We recorded 100 whole-brain volumes at a resolution of $0.49 \times 0.49 \times 1$ μm ($1{,}024 \times 512 \times 300$ XYZ voxels), to a sample depth of 300 μm. The microscope was controlled by ScanImage.

Creation of the FDA. Each anatomical scan was created by first imaging the myr-tdTomato signal 100 times at $0.6 \times 0.6 \times 1$ μm ($1{,}024 \times 512 \times 241$ XYZ voxels). These 100 volumes were averaged, then each volume was warped (linear and nonlinear) to this mean using ANTs, thereby correcting for motion. These aligned volumes were then averaged, creating the anatomical scan for each brain. Scans were additionally processed with an intensity-based masking (to remove any contaminating background signal outside of the brain), removal of noncontiguous blobs (to remove, for example, cuticle which is otherwise visible due to autofluorescence), and histogram equalization to brighten overly dark areas and darken overly bright areas (which assists in allowing a more uniform registration, and not an overemphasis on simply the brightest regions). Each brain was mirrored across the Y axis, doubling our effective data to 32 brains. These 32 brains were all linearly aligned to a single seed brain chosen from the 32, and averaged ("linear0"). The 32 brains were linearly aligned to "linear0," and again averaged, producing "linear1." Next, the individual anatomical scans were sharpened using the scikit-image implementation of unsharp masking, and aligned again (linear and nonlinear) to "linear," and averaged to produced "SyN0." The last step was repeated two more times to produce the final FDA. We found that sharpening the brains before "linear0" caused poor convergence of neuropil boundaries, while completely omitting it resulted in blurry neuropil boundaries.

The BIFROST Pipeline. The BIFROST pipeline comprises four steps. First, a dataset template is created from structural volumes from each animal. Second, this dataset template is registered to the FDA. Third, each time point from each dependent channel is registered to the dataset template. Finally, these registered data are transformed into FDA space using the transformation calculated on step two.

We provide the BIFROST pipeline as a Snakemake workflow that describes the dependency structure of the whole pipeline (64). This facilitates parallel execution of independent steps, and as a result BIFROST can be transparently scaled from local execution on a single machine to thousands of parallel jobs on a cluster. This parallelization is critical, because serial execution of the ANTs dependent steps over such large datasets would take weeks to months to complete. BIFROST can be executed on all common cluster scheduling systems including Slurm, PBS (Portable Batch System), and GSE (Grid Sun Engine) and on cloud services via Kubernetes and several common cloud APIs (64). This implementation allows a dataset over any number of animals with any number of channels, each imaged for an arbitrary number of time points and stored following a particular directory structure to be quickly submitted to a cluster for parallel execution with only minimal customization.

The BIFROST pipeline: Creation of dataset templates. Dataset templates were constructed from structural volumes of each animal following a standard procedure (34). These volumes were mirrored, doubling the effective sample size, and preprocessed with the scikit-image implementation of contrast-limited adaptive histogram equalization (CLAHE) using a kernel size of 64 (65, 66). Template construction begins with a single volume, chosen arbitrarily from the preprocessed volumes to serve as the initial template. Linear (affine) transformations then aligned each preprocessed image to this initial template. Next, the transformed volumes were averaged to obtain a new template. Following this linear iteration, template construction continued with several (typically four) iterations of nonlinear alignment and averaging. In each iteration, individual images were nonlinearly transformed to the current template using SyN. Next, the transformed volumes were averaged to obtain a mean volume and the transformations themselves were also averaged. To complete each iteration, the next template is obtained by transforming the mean volume through the inverse of the mean transformation (67, 68). The fourth iteration of this cycle produces the final dataset template. The pipeline is outlined in *SI Appendix*, Fig. S1*B*. We have released our tooling for template construction as part of our Python package.

The BIFROST pipeline: Registration with SynthMorph. We wrote a configurable tool for image registration which registers a "moving" image to a "fixed" image with successive linear, nonlinear SyN, and SynthMorph transforms. If necessary, both "moving" and "fixed" images can be downsampled to reduce memory burden and computation time. As we found that SynthMorph was essential to effective registration in the central brain, but not the optic lobes, we also added support for masking the SynthMorph transform and manually generated a mask for the optic lobes using FIJI/ImageJ (69). Next, we preprocessed the "moving" and "fixed" images by rescaling intensities to the interval $[0, 1]$ and applied the scikit-image implementation of CLAHE (65, 66) with a kernel size of 64 and configurable clip limit. By default CLAHE was applied to the "moving" image but can be applied to the "fixed" image as well.

After this preprocessing, linear (affine) and nonlinear (SyN) transforms registering the "moving" image to the "fixed" image were computed and applied in sequence using ANTs.

Next, a nonlinear SynthMorph transform was computed. As SynthMorph is constrained by its architecture to a fixed inference volume of $160 \times 160 \times 192$ voxels, images were first transposed to align the longest axis of the image with that of the inference volume and then downsampled to $160 \times 160 \times 192$ voxels. Finally, SynthMorph inference was run on the downsampled images yielding a warp field.

Next, the warp field was transposed back to the original axis order and then optionally mirror symmetrized across an algorithmically selected mirror plane, obtained by searching for the plane that minimizes the root mean square distance between the "moving" image and its mirror. This was performed on the "moving" image after it was affine transformed to the "fixed" image. In our experience, when the, "fixed" image is aligned such that the dorsal–ventral axis lies along a principal axis of voxel coordinates this procedure reliably recovers the intended dorsal–ventral/anterior–posterior mirror plane of the *Drosophila* brain.

Next, the (optional) mask was transformed through the linear and nonlinear transformations. The warp field was then up-sampled to the original size of the images and applied to the "moving" image at all locations outside the mask, yielding the final image. The pipeline is outlined in *SI Appendix*, Fig. S1*C*. All transformations and meta-data needed to apply the full transform were saved in a HDF5 file (70). All tooling for computing registrations and applying the resulting transforms are provided as part of our Python package.

Manual Segmentation of Neuropils. We used ITK-SNAP to manually draw regions of interest in an early version of the FDA, and then registered into the final FDA (71). We used ITK-SNAP's built-in contrast-based segmentation to delineate the boundaries of the whole brain. We then hand-segmented the mushroom bodies (calyx, peduncles, ventral lobes, and medial lobes), central complex (protocerebral bridge), and optic lobes in each z-slice of the volume.

Calculation of Sørenson–Dice Coefficients for the Cross-Modal Quantification. Region of interest annotations in the space of JRC2018F were obtained by registering a previous template that was published with regional annotations into the space of JRC2018F (28). Correspondences between these ROIs and those annotated in the FDA were identified manually. Given sets X and Y, the Sørenson–Dice coefficient is defined as

$$\frac{2|X \cap Y|}{|X| + |Y|}$$

where $|X|$ and $|Y|$ are the cardinalities of the sets. The Sørenson–Dice coefficient was computed for each ROI in a voxel-wise manner.

Defining the Positions of LC11 and DSX Centroids. After alignment, whole-brain volumes were cropped to a region that contained the feature of interest (the terminal glomerulus for LC11, and a specific stalk for DSX). Box size was 95 × 57 × 76 μm for LC11, and 38 × 30 × 23 μm for DSX. In addition, for LC11, fluorescence outside of the PLP and PVLP regions was masked using the anatomical ROIs to avoid expression from LC11 dendrites in the lobula. An intensity threshold was then manually selected for each animal that best removed background fluorescence while maintaining the shape of the glomerulus. The image was then binarized and the center of mass determined

Subvolume Alignment. We started with the same 9 flies from Lab 1 that were used to produce the results in Fig. 3, and cropped each brain to a 95 × 95 × 38 μm subvolume (Lateral–Medial, Dorsal–Ventral, and Anterior–Posterior) that contained the LC11 glomerulus from a single hemisphere (resulting in 18 subvolumes). The location of the bounding-box for each subvolume was selected directly from each individual brain, without selecting precisely the same subvolume position, simulating the practical collection of subvolumes with slightly varied positions. A dataset template was created using BIFROST using these 18 subvolumes. Before aligning the subvolume dataset template to the FDA using BIFROST, we performed a simple but critical manual step, which users attempting to align subvolumes to the FDA must also perform. The goal of this step is to crudely and manually visually match the spatial position of the subvolume dataset template within the FDA. That is, BIFROST must be provided with an initial estimate of the location of the subvolume within the FDA. In practice, this is best achieved by visualizing the center point of the subvolume dataset template; to do this, we displayed the center z-slice of the dataset template in a Python Jupyter notebook, and drew centered cross-hairs along the remaining two axes. Next, we manually navigated to the z-slice of the FDA which visually best contained the same z-slice of the dataset template, and drew cross-hairs along the remaining two axes in the position that best matched the cross-hairs of the subvolume dataset template. With an estimate of the x,y,z location of the center of the subvolume dataset template within the FDA, we then cropped the FDA to match the location and spatial size of the subvolume dataset template, and saved this cropped FDA. Finally, we used BIFROST to register the subvolume dataset template to the cropped FDA.

Aligning JRC2018F and Connectomes to the FDA. The coordinates of the skeleton and synapses of LC11 were fetched from the online resources for the Hemibrain and FlyWire and were transformed into the space of JRC2018F using the flybrains Python package (30, 33, 34, 72–75). In the flybrains package, the coordinate systems for the Hemibrain and FlyWire are labeled as "JRCFIB2018Fraw" and "FLYWIRE" respectively. These data were further transformed from JRC2018F into the space of the FDA by application of a bridging transformation, as follows. First, we applied the BIFROST pipeline to transform JRC2018F to the FDA (*The BIFROST Pipeline: Registration with SynthMorph*). We next wished to apply this transformation to the connectomes. However, SynthMorph does not support coordinate transformations, which is required for a connectome. Therefore, we recapitulated the full BIFROST transformation using only ANTs. We achieved this as follows. First, the FDA was transformed to JRC2018F using BIFROST. This FDA in JRC2018F space is now our new "fixed" target. Since this is now a single modality problem, we were then able to use ANTs to transform the original FDA to this fixed target. The pipeline is outlined in *SI Appendix*, Fig. S1*D*.

Data, Materials, and Software Availability. FDA, bridging transforms and a replication dataset, and Software have been deposited in Dryad; Zenodo (https://doi.org/10.5061/dryad.8pk0p2nx1 (76); https://zenodo.org/doi/10.5281/zenodo.11097259 (77)).

ACKNOWLEDGMENTS. We would like to thank members of the Murthy and Clandinin labs for helpful discussions. We would also like to thank Gregory Jefferis for sharing his advice, as well as Niyathi Annamaneni for help with figure design. O.M.A. was supported by the Burroughs Wellcome Fund Postdoctoral Enrichment Program, the Broadening the Representation of Academic Investigators in NeuroScience Fellowship, the Simons Collaboration on the Global Brain Bridge to Independence Award, and the Princeton Presidential Postdoctoral Fellowship. B.E.B. was supported by a NSF Graduate Research Fellowship. Y.A.H. was supported by a Stanford Bio-X Bowes Fellowship. A.L. was supported by the NSF through the Center for the Physics of Biological Function (PHY-1734030). This work was supported by NIH NINDS R35 to M.M., R01EY022638 to T.R.C., NIH BRAIN R01 NS110060 to M.M. and T.R.C., Simons Collaboration of the Global Brain award to M.M. and T.R.C. T.R.C. is a Chan-Zuckerberg BioHub Investigator.

Author affiliations: [a]Department of Neurobiology, Stanford University, Stanford, CA 94305; [b]Princeton Neuroscience Institute, Princeton University, Princeton, NJ 08544; [c]Department of Physics, University of Colorado Boulder, Boulder, CO 80302; [d]Department of Bioengineering, Stanford University, Stanford, CA 94305; [e]Center for the Physics of Biological Function, Princeton University, Princeton, NJ 08544; [f]Department of Psychology, University of Washington, Seattle, WA; and [g]Department of Neurobiology, Harvard Medical School, Boston, MA 02115

Author contributions: B.E.B., M.M., and T.R.C. designed research; B.E.B., Y.A.H., A.L., O.M.A., and D.A.P. performed research; S.Y.T. contributed new reagents/analytic tools; B.E.B., A.B.B., Y.A.H., A.L., and O.M.A. analyzed data; B.E.B., Y.A.H., and B.E.B. wrote software; and B.E.B., A.B.B., Y.A.H., A.L., O.M.A., and T.R.C. wrote the paper.

1. S. Kato *et al.*, Global brain dynamics embed the motor command sequence of *Caenorhabditis elegans*. *Cell* **163**, 656–669 (2015).
2. H. S. Kaplan, O. Salazar Thula, N. Khoss, M. Zimmer, Nested neuronal dynamics orchestrate a behavioral hierarchy across timescales. *Neuron* **105**, 562–576 (2020).
3. E. Yemini *et al.*, A multicolor atlas for whole-brain neuronal identification in *C. elegans*. *Cell* **184**, 272–288 (2021).
4. V. Susoy *et al.*, Natural sensory context drives diverse brain-wide activity during *C. elegans* mating. *Cell* **184**, 5122–5137.e17 (2021).
5. K. M. Hallinen *et al.*, Decoding locomotion from population neural activity in moving *C. elegans*. *eLife* **10**, e66135 (2021).
6. A. Lin *et al.*, Imaging whole-brain activity to understand behaviour. *Nat. Rev. Phys.* **4**, 292–305 (2022).
7. M. B. Ahrens, M. B. Orger, D. N. Robson, J. M. Li, P. J. Keller, Whole-brain functional imaging at cellular resolution using light-sheet microscopy. *Nat. Methods* **10**, 413–420 (2013).
8. T. W. Dunn *et al.*, Brain-wide mapping of neural activity controlling zebrafish exploratory locomotion. *eLife* **5**, 1–29 (2016).

9. M. Haesemeyer, D. N. Robson, J. M. Li, A. F. Schier, F. Engert, A brain-wide circuit model of heat-evoked swimming behavior in larval zebrafish. *Neuron* **98**, 817–831 (2018).
10. G. C. Vanwalleghem, M. B. Ahrens, E. K. Scott, Integrative whole-brain neuroscience in larval zebrafish. *Curr. Opin. Neurobiol.* **50**, 136–145 (2018).
11. X. Chen *et al*., Brain-wide organization of neuronal activity and convergent sensorimotor transformations in larval zebrafish. *Neuron* **100**, 876–890 (2018).
12. K. Mann, C. L. Gallen, T. R. Clandinin, Whole-brain calcium imaging reveals an intrinsic functional network in *Drosophila*. *Curr. Biol.* **27**, 2389–2396 (2017).
13. S. Aimon *et al*., Fast near-whole-brain imaging in adult *Drosophila* during responses to stimuli and behavior. *PLoS Biol.* **17**, e2006732 (2019).
14. K. Mann, S. Deny, S. Ganguli, T. R. Clandinin, Coupling of activity, metabolism and behaviour across the *Drosophila* brain. *Nature* **593**, 244–248 (2021).
15. D. A. Pacheco, S. Y. Thiberge, E. Pnevmatikakis, M. Murthy, Auditory activity is diverse and widespread throughout the central brain of *Drosophila*. *Nat. Neurosci.* **24**, 93–104 (2021).
16. B. E. Brezovec *et al*., Mapping the neural dynamics of locomotion across the *Drosophila* brain. *Curr. Biol.* **34**, 710–726.e4 (2024).
17. S. Aimon, K. Y. Cheng, J. Gjorgjieva, I. C. G. Kadow, Global change in brain state during spontaneous and forced walk in *Drosophila* is composed of combined activity patterns of different neuron classes. *eLife* **12**, e85202 (2023).
18. E. S. Schaffer *et al*., The spatial and temporal structure of neural activity across the fly brain. *Nat. Com.* **14**, 5572 (2023).
19. J. Demas *et al*., High-speed, cortex-wide volumetric recording of neuroactivity at cellular resolution using light beads microscopy. *Nat. Methods* **18**, 1103–1111 (2021).
20. O. Randlett *et al*., Whole-brain activity mapping onto a zebrafish brain atlas. *Nat. methods* **12**, 1039–1046 (2015).
21. M. Kunst *et al*., A cellular-resolution atlas of the larval zebrafish brain. *Neuron* **103**, 21–38 (2019).
22. S. W. Oh *et al*., A mesoscale connectome of the mouse brain. *Nature* **508**, 207–214 (2014).
23. K. Amunts, H. Mohlberg, S. Bludau, K. Zilles, Julich-brain: A 3D probabilistic atlas of the human brain's cytoarchitecture. *Science* **369**, 988–992 (2020).
24. Y. Xiao *et al*., Evaluation of MRI to ultrasound registration methods for brain shift correction: The curious2018 challenge. *IEEE Trans. Med. Imaging* **39**, 777–786 (2019).
25. J. P. Pluim, J. A. Maintz, M. A. Viergever, Mutual-information-based registration of medical images: A survey. *IEEE Trans. Med. Imaging* **22**, 986–1004 (2003).
26. L. Qu *et al*., Cross-modal coherent registration of whole mouse brains. *Nat. Methods* **19**, 111–118 (2022).
27. D. Münch, D. Goldschmidt, C. Ribeiro, The neuronal logic of how internal states control food choice. *Nature* **607**, 747–755 (2022).
28. A. Jenett *et al*., A gal4-driver line resource for *Drosophila* neurobiology. *Cell Rep.* **2**, 991–1001 (2012).
29. I. Arganda-Carreras *et al*., A statistically representative atlas for mapping neuronal circuits in the *Drosophila* adult brain. *Front. Neuroinf.* **12**, 13 (2018).
30. K. Ito *et al*., A systematic nomenclature for the insect brain. *Neuron* **81**, 755–765 (2014).
31. K. Rein, M. Zöckler, M. T. Mader, C. Grübel, M. Heisenberg, The *Drosophila* standard brain. *Curr. Biol.* **12**, 227–231 (2002).
32. Z. Zheng *et al*., A complete electron microscopy volume of the brain of adult *Drosophila melanogaster*. *Cell* **174**, 730–743.e22 (2018).
33. B. As *et al*., The natverse, a versatile toolbox for combining and analysing neuroanatomical data. *eLife* **9**, e53350 (2020).
34. J. A. Bogovic *et al*., An unbiased template of the *Drosophila* brain and ventral nerve cord. *PLoS One* **15**, e0236495 (2020).
35. B. D. Pfeiffer *et al*., Tools for neuroanatomy and neurogenetics in *Drosophila*. *Proc. Natl. Acad. Sci. U.S.A.* **105**, 9715–9720 (2008).
36. A. Jenett *et al*., A gal4-driver line resource for *Drosophila* neurobiology. *Cell Rep.* **2**, 991–1001 (2012).
37. G. W. Meissner *et al*., A searchable image resource of *Drosophila* GAL4-driver expression patterns with single neuron resolution. *eLife* **12**, e80660 (2023).
38. L. K. Scheffer *et al*., A connectome and analysis of the adult *Drosophila* central brain. *elife* **9**, e57443 (2020).
39. S. Dorkenwald *et al*., Flywire: Online community for whole-brain connectomics. *Nat. Methods* **19**, 119–128 (2022).
40. S. Dorkenwald *et al*., Neuronal wiring diagram of an adult brain. *Nature* **634**, 124–138 (2024).
41. H. Peng *et al*., Brainaligner: 3D registration atlases of *Drosophila* brains. *Nat. Methods* **8**, 493–498 (2011).
42. J. Clements *et al*., Neuronbridge: An intuitive web application for neuronal morphology search across large data sets. *BMC Bioinformatics* **25**, 114 (2024).
43. B. B. Avants *et al*., A reproducible evaluation of ants similarity metric performance in brain image registration. *Neuroimage* **54**, 2033–2044 (2011).
44. B. B. Avants, C. L. Epstein, M. Grossman, J. C. Gee, Symmetric diffeomorphic image registration with cross-correlation: Evaluating automated labeling of elderly and neurodegenerative brain. *Med. Image Anal.* **12**, 26–41 (2008).
45. A. Klein *et al*., Evaluation of 14 nonlinear deformation algorithms applied to human brain MRI registration. *Neuroimage* **46**, 786–802 (2008).
46. Y. Fu *et al*., Deep learning in medical image registration: A review. *Phys. Med. Biol.* **65**, 20TR01 (2020).
47. X. Yang, R. Kwitt, M. Styner, M. Niethammer, Quicksilver: Fast predictive image registration - a deep learning approach. *Neuroimage* **158**, 378–396 (2017).
48. J. A. Bogovic, P. Hanslovsky, A. Wong, S. Saalfeld, "Robust registration of calcium images by learned contrast synthesis" in *2016 IEEE 13th International Symposium on Biomedical Imaging (ISBI)* (IEEE, 2016), pp. 1123–1126.
49. M. Hoffmann *et al*., Synthmorph: Learning contrast-invariant registration without acquired images. *IEEE Trans. Med. Imaging* **41**, 543–558 (2021).
50. T. Rohlfing, Image similarity and tissue overlaps as surrogates for image registration accuracy: Widely used but unreliable. *IEEE Trans. Med. Imaging* **31**, 153–163 (2011).
51. T. A. Sørensen, A method of establishing groups of equal amplitude in plant sociology based on similarity of species content and its application to analyses of the vegetation on danish commons. *Biol. Skr.* **5**, 1–34 (1948).
52. L. R. Dice, Measures of the amount of ecologic association between species. *Ecology* **26**, 297–302 (1945).
53. L. K. Scheffer *et al*., A connectome and analysis of the adult *Drosophila* central brain. *eLife* **9**, 1–74 (2020).
54. J. G.S. *et al*., Comprehensive maps of drosophila higher olfactory centers: Spatially segregated fruit and pheromone representation. *Cell* **128**, 1187–1203 (2007).
55. M. H. Turner, A. Krieger, M. M. Pang, T. R. Clandinin, Visual and motor signatures of locomotion dynamically shape a population code for feature detection in *Drosophila*. *eLife* **11**, e82587 (2022).
56. M. H. Turner, K. Mann, T. R. Clandinin, The connectome predicts resting-state functional connectivity across the *Drosophila* brain. *Curr. Biol.* **31**, 2386–2394 (2021).
57. A. Lin *et al*., Network statistics of the whole-brain connectome of Drosophila. *Nature* **634**, 153–165 (2024).
58. P. Schlegel *et al*., Whole-brain annotation and multi-connectome cell typing quantifies circuit stereotypy in Drosophila. *Nature* **634**, 139–152 (2024).
59. J. Ib *et al*., SPARC enables genetic manipulation of precise proportions of cells. *Nat. Neurosci.* **23**, 1168–1175 (2020).
60. F. Randi, A. K. Sharma, S. Dvali, A. M. Leifer, Neural signal propagation atlas of *Caenorhabditis elegans*. *Nature* **2023**, 1–9 (2023).
61. J. K. Lappalainen *et al*., Connectome-constrained networks predict neural activity across the fly visual system. *Nature* (2024). https://doi.org/10.1038/s41586-024-07939-3.
62. L. Mi *et al*., "Connectome-constrained latent variable model of whole-brain neural activity" in *International Conference on Learning Representations* (2021).
63. P. Schlegel *et al*., Information flow, cell types and stereotypy in a full olfactory connectome. *eLife* **10**, e66018 (2021).
64. F. Mölder *et al*., Sustainable data analysis with snakemake. *F1000Research* **10**, 33 (2021).
65. S. van der Walt *et al*., scikit-image: Image processing in Python. *PeerJ* **2**, e453 (2014).
66. K. Zuiderveld, "Contrast limited adaptive histogram equalization" in *Graphics Gems*, P. S. Heckbert, Ed. (Academic Press, 1994), pp. 474–485.
67. B. Avants, J. C. Gee, Geodesic estimation for large deformation anatomical shape averaging and interpolation. *Neuroimage* **23**, S139–S150 (2004).
68. B. B. Avants *et al*., The optimal template effect in hippocampus studies of diseased populations. *Neuroimage* **49**, 2457–2466 (2010).
69. J. Schindelin *et al*., Fiji: An open-source platform for biological-image analysis. *Nat. Methods* **9**, 676–682 (2012).
70. T. H. Group, Hierarchical data format, version 5 (1997–2023). https://www.hdfgroup.org/HDF5/ Accessed 18 May 2023.
71. P. A. Yushkevich *et al*., User-guided 3D active contour segmentation of anatomical structures: Significantly improved efficiency and reliability. *Neuroimage* **31**, 1116–1128 (2006).
72. S. M. Plaza *et al*., neu print: An open access tool for EM connectomics. *Front. Neuroinf.* **16**, 896292 (2022).
73. A. Matsliah *et al*., codex (2023) https://codex.flywire.ai/; 10.13140/RG.2.2.35928.67844. Deposited 3 October 2023.
74. P. Schlegel, R. Court, navis-org/navis-flybrains: Version 0.3.0 (v0.3.0). Zenodo (2024). 10.5281/zenodo.13694265. Deposited 5 September 2024.
75. J. S. Phelps *et al*., Reconstruction of motor control circuits in adult *Drosophila* using automated transmission electron microscopy. *Cell* **184**, 759–774 (2021).
76. B. E. Brezovec *et al*., BIFROST: A method for registering diverse imaging datasets. Dryad. https://doi.org/10.5061/dryad.8pk0p2nx1. Deposited 21 May 2024.
77. B. E. Brezovec *et al*., BIFROST. Zenodo. https://zenodo.org/doi/10.5281/zenodo.11097259. Deposited 29 May 2024.